Geophysical Journal International

Geophys. J. Int. (2016) **206,** 1552–1562
Advance Access publication 2016 June 15
GJI Geodynamics and tectonics

doi: 10.1093/gji/ggw229

A hybrid boundary-integral/thin-sheet equation for subduction modelling

Bingrui Xu and Neil M. Ribe

Laboratoire FAST, Univ Paris-Saclay, Univ Paris-Sud, CNRS Bâtiment 502, 6 *rue du Belvédère F*-91405 *Orsay, France. E-mail: ribe@fast.u-psud.fr*

Accepted 2016 June 13. Received 2016 June 10; in original form 2016 March 10

SUMMARY

Subducting oceanic lithosphere is an example of a thin sheet-like object whose characteristic lateral dimension greatly exceeds its thickness. Here we exploit this property to derive a new hybrid boundary-integral/thin sheet (BITS) representation of subduction that combines in a single equation all the forces acting on the sheet: gravity, internal resistance to bending and stretching, and the tractions exerted by the ambient mantle. For simplicity, we limit ourselves to 2-D. We solve the BITS equations using a discrete Lagrangian approach in which the sheet is represented by a set of vertices connected by edges. Instantaneous solutions for the sinking speed of a slab attached to a trailing flat sheet obey a scaling law of the form $V/V_{\rm Stokes} = {\rm fct(St)}$, where $V_{\rm Stokes}$ is a characteristic Stokes sinking speed and St is the sheet's flexural stiffness. Time-dependent solutions for the evolution of the sheet's shape and thickness show that these are controlled by the viscosity ratio between the sheet and its surroundings. An important advantage of the BITS approach is the possibility of generalizing the sheet's rheology, either to a viscosity that varies along the sheet or to a non-Newtonian shear-thinning rheology.

Key words: Planetary tectonics; Subduction zone processes; Dynamics of lithosphere and mantle.

1 INTRODUCTION

Subduction is a crucial part of Earth's plate tectonic cycle, and consists in the sinking of cold and dense oceanic lithosphere into the hotter and less viscous mantle below. Strictly speaking, a subducted slab is not a distinct object because physical properties such as temperature and viscosity vary continuously between the slab and its surroundings. However, the gradients of these properties are sufficiently large that it makes sense to model the slab as an object whose properties are distinct from those of its surroundings. Such 'two-fluid' models have been widely used in analogue laboratory experiments, where a sheet of silicone putty or very viscous glucose syrup is made to subduct in a tank filled with glucose syrup having a much lower viscosity (Kincaid & Olson 1987; Griffiths *et al.* 1995; Guillou-Frottier *et al.* 1995; Funiciello *et al.* 2003, 2004, 2008; Schellart 2004a,b, 2008; Bellahsen *et al.* 2005; Martinod *et al.* 2005; Faccenna *et al.* 2007).

Two-fluid models have also been implemented numerically using the boundary-element method (BEM), which is especially well adapted to tracking the interface between two fluids with different viscosities (Morra *et al.* 2006, 2007; Ribe 2010; Li & Ribe 2012). Other advantages of the BEM include a total absence of undesired wall effects and a reduction of the dimensionality of the problem by 1 (from 3-D to 2-D or 2-D to 1-D). Ribe (2010) and Li & Ribe (2012) used 2-D and 3-D BEM models, respectively, to study the buoyancy-driven subduction of a thin viscous sheet in a second fluid with a much smaller viscosity. Scaling laws for the sinking speed of the slab's leading edge were obtained by interpreting the raw BEM output in terms of thin viscous-sheet theory.

In the studies of Ribe (2010) and Li & Ribe (2012), thin-sheet theory was used *a posteriori* as an interpretive tool to understand the results of full BEM simulations. It is therefore natural to ask whether a method can be developed in which thin-sheet theory is built in from the start. It turns out that the answer is yes. The result is a hybrid boundary-integral/thin-sheet (BITS) integral equation that combines thin-sheet theory with a boundary-integral representation of the flow in the surrounding fluid. After deriving the new model in the next section of this paper, we introduce a Lagrangian description of the sheet's geometry and kinematics. Finally, we formulate a discrete (as opposed to smooth) solution procedure based on concepts from discrete differential geometry and present some representative solutions for the subduction of thin sheets.

2 BOUNDARY-INTEGRAL EQUATION FOR AN IMMERSED FLUID SHEET

Fig. 1 shows the situation that we shall study. A viscous sheet with viscosity η_2 and density $\rho_1 + \delta\rho$ is immersed in a fluid half-space with viscosity η_1 and density ρ_1. The sheet of length L comprises a flat trailing portion (the 'plate') of length $L - \ell$ and a bent sinking portion (the 'slab') of length ℓ. Positions on the sheet's mid-surface are parametrized by the arclength $s \in [0, L(t)]$. Initially, the sheet's thickness is h (constant). However, during progressive subduction

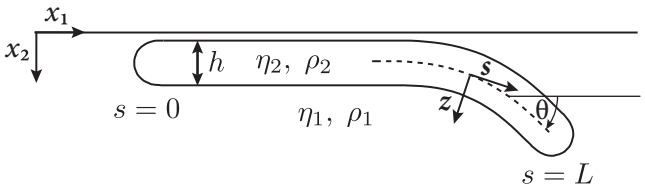

Figure 1. Definition sketch of the subduction model. The BITS model discretizes only the mid-surface of the sheet (dashed line), while the BEM discretizes the entire sheet/ambient fluid interface, including the sheet's rounded ends.

the sheet undergoes non-uniform stretching and compression, which makes its thickness $h(s, t)$ non-uniform and time-dependent.

It may appear at first sight that our model is vitiated by Stokes's paradox, which states that a 2-D solution of Stokes's equations for the flow around a cylinder in an infinite fluid does not exist. However, when a boundary is present, the downward buoyancy force exerted by the cylinder on the fluid is exactly balanced by the integrated normal stress over the boundary. The net force on the fluid is thus zero, and Stokes's paradox is resolved. This result holds for a cylinder of any viscosity and cross-sectional shape. A solution of our model problem therefore exists.

Let S_1 and S_2 be the areas occupied by fluids 1 and 2, respectively, and let C be the interface between them. The general integral representations for the flows in fluids 1 and 2 are (Ladyzhenskaya 1969):

$$-\frac{1}{\eta_1}\int_C \boldsymbol{f}_1(\boldsymbol{y})\cdot\boldsymbol{J}(\boldsymbol{y}-\boldsymbol{x})\mathrm{d}\ell(\boldsymbol{y}) + \int_C \boldsymbol{u}_1(\boldsymbol{y})\cdot\boldsymbol{K}(\boldsymbol{y}-\boldsymbol{x})\cdot\boldsymbol{n}(\boldsymbol{y})\mathrm{d}\ell(\boldsymbol{y}) = \chi_1(\boldsymbol{x})\boldsymbol{u}_1(\boldsymbol{x}), \tag{1}$$

$$\frac{1}{\eta_2}\int_C \boldsymbol{f}_2(\boldsymbol{y})\cdot\boldsymbol{J}(\boldsymbol{y}-\boldsymbol{x})\mathrm{d}\ell(\boldsymbol{y}) - \int_C \boldsymbol{u}_2(\boldsymbol{y})\cdot\boldsymbol{K}(\boldsymbol{y}-\boldsymbol{x})\cdot\boldsymbol{n}(\boldsymbol{y})\mathrm{d}\ell(\boldsymbol{y}) = \chi_2(\boldsymbol{x})\boldsymbol{u}_2(\boldsymbol{x}), \tag{2}$$

where $\boldsymbol{J}$ and $\boldsymbol{K}$ are the velocity and stress Green functions for Stokes flow satisfying the boundary conditions on the surface of the fluid half-space. The quantity $\chi_1(\boldsymbol{x}) = 1, 1/2$ or 0 if $\boldsymbol{x}$ is in S_1, right on the contour, or in S_2, respectively, and $\chi_2(\boldsymbol{x})$ is defined similarly with the subscripts 1 and 2 interchanged. The unit normal vector $\boldsymbol{n}$ is directed out of fluid 2 and into fluid 1.

On the contour C, the velocity is continuous while the modified normal stress undergoes a jump proportional to the difference of the densities of the two fluids. Symbolically,

$$\boldsymbol{u}_1 = \boldsymbol{u}_2, \tag{3}$$

$$\boldsymbol{f}_2(\boldsymbol{y}) = \boldsymbol{f}_1(\boldsymbol{y}) + \delta\rho(\boldsymbol{g}\cdot\boldsymbol{y})\boldsymbol{n}. \tag{4}$$

Now add eqs (1) and (2) and use the matching condition (3) to obtain

$$\chi_1(\boldsymbol{x})\boldsymbol{u}_1(\boldsymbol{x}) + \chi_2(\boldsymbol{x})\boldsymbol{u}_2(\boldsymbol{x}) = \int_C \left(\frac{\boldsymbol{f}_2}{\eta_2} - \frac{\boldsymbol{f}_1}{\eta_1}\right)\cdot\boldsymbol{J}(\boldsymbol{y}-\boldsymbol{x})\mathrm{d}\ell, \tag{5}$$

where $\mathrm{d}\ell(\mathbf{y})$ has been shortened to $\mathrm{d}\ell$. Then apply eq. (4) to obtain

$$\chi_1(\boldsymbol{x})\boldsymbol{u}_1(\boldsymbol{x}) + \chi_2(\boldsymbol{x})\boldsymbol{u}_2(\boldsymbol{x}) = \frac{1-\gamma}{\eta_2}\int_C \boldsymbol{f}_1\cdot\boldsymbol{J}(\boldsymbol{y}-\boldsymbol{x})\mathrm{d}\ell + \frac{\delta\rho}{\eta_2}\int_C (\boldsymbol{g}\cdot\boldsymbol{y})\boldsymbol{n}\cdot\boldsymbol{J}(\boldsymbol{y}-\boldsymbol{x})\mathrm{d}\ell, \tag{6}$$

where $\gamma = \eta_2/\eta_1$ is the viscosity ratio. Evaluate on the mid-surface $\boldsymbol{x} = \boldsymbol{X}$ to obtain

$$\boldsymbol{U}(\boldsymbol{X}) = \frac{1-\gamma}{\eta_2}\int_C \boldsymbol{f}_1\cdot\boldsymbol{J}(\boldsymbol{y}-\boldsymbol{X})\mathrm{d}\ell + \frac{\delta\rho}{\eta_2}\int_C (\boldsymbol{g}\cdot\boldsymbol{y})\boldsymbol{n}\cdot\boldsymbol{J}(\boldsymbol{y}-\boldsymbol{X})\mathrm{d}\ell. \tag{7}$$

To simplify the first integral in eq. (7), we note that in the limit $h/L \equiv \epsilon \to 0$ the kernel $\mathbf{J}(\mathbf{y}-\mathbf{x})$ on both the upper and lower surfaces of the sheet is approximately equal to its value $\mathbf{J}(\mathbf{y}-\mathbf{X})$ on the sheet's mid-surface. Ignoring the small regions of size $O(h)$ near the ends of the sheet, we may write

$$\int_C \mathbf{f}_1\cdot\mathbf{J}(\mathbf{y}-\mathbf{X})\mathrm{d}\ell \approx \int_{C_+} \mathbf{f}_+\cdot\mathbf{J}(\mathbf{y}-\mathbf{X})\mathrm{d}\ell + \int_{C_-} \mathbf{f}_-\cdot\mathbf{J}(\mathbf{y}-\mathbf{X})\mathrm{d}\ell$$

$$\approx \int_0^L \left[\mathbf{f}_1^+(p) + \mathbf{f}_1^-(p)\right]\cdot\mathbf{J}(\mathbf{X}(p)-\mathbf{X}(s))\mathrm{d}p, \tag{8}$$

where p is a dummy variable of integration representing arclength along the mid-surface.

The forces acting on the sheet are the internal viscous forces, gravity, and the tractions applied by the outer fluid. Finally, the force balance per unit length ds for a thin viscous sheet is

$$\boldsymbol{N}' + \boldsymbol{g}h\delta\rho + \boldsymbol{f}_1^+ + \boldsymbol{f}_1^- = 0, \tag{9}$$

where $\boldsymbol{f}_1^{\pm}$ are the tractions exerted on the surfaces $z = \pm h/2$ by the external fluid and $\boldsymbol{g}$ is the gravitational acceleration. Substituting the force balance (9) into eq. (8) yields

$$\int_C \mathbf{f}_1\cdot\mathbf{J}(\mathbf{y}-\mathbf{X})\mathrm{d}\ell \approx -\int_0^L \left[\boldsymbol{N}' + h\delta\rho\mathbf{g}\right]\cdot\mathbf{J}(\mathbf{X}(p)-\mathbf{X}(s))\mathrm{d}p. \tag{10}$$

To simplify the second integral in eq. (7), we convert it to a surface integral using the divergence theorem and expand the derivative under the integral sign to obtain

$$\int_C (\mathbf{g}\cdot\mathbf{y})\mathbf{n}\cdot\mathbf{J}(\mathbf{y}-\mathbf{X})\mathrm{d}\ell = \int_{S_2} \mathbf{g}\cdot\mathbf{J}(\mathbf{y}-\mathbf{X})\mathrm{d}S_2 + \int_{S_2} (\mathbf{g}\cdot\mathbf{y})\nabla\cdot\mathbf{J}(\mathbf{y}-\mathbf{X})\mathrm{d}S_2. \tag{11}$$

In the second integral on the right side of eq. (11), $y \sim h$ and $\nabla \sim L^{-1}$, except for points $\mathbf{y}$ close to $\mathbf{X}$. This implies that the second integral is of order $h/L \ll 1$ relative to the first integral on the right side. So the second integral can therefore be neglected. Now the first integral can be approximated as an integral along the mid-surface over a distribution of Stokeslets with density $h\mathbf{g}$ per unit mid-surface length. We thereby obtain

$$\int_C (\mathbf{g}\cdot\mathbf{y})\mathbf{n}\cdot\mathbf{J}(\mathbf{y}-\mathbf{X})\mathrm{d}\ell \approx \int_{S_2} \mathbf{g}\cdot\mathbf{J}(\mathbf{y}-\mathbf{X})\mathrm{d}S_2 \approx \int_0^L h\mathbf{g}\cdot\mathbf{J}(\mathbf{X}(p)-\mathbf{X}(s))\mathrm{d}p. \tag{12}$$

Substituting eqs (10) and (12) into eq. (7), we obtain the BITS equation

$$\mathbf{U}(s) = \frac{1}{\eta_2}\int_0^L \left[\gamma\mathbf{g}h(p)\delta\rho + (\gamma-1)\mathbf{N}'(p)\right]\cdot\mathbf{J}(\mathbf{X}(p)-\mathbf{X}(s))\mathrm{d}p, \tag{13}$$

where $\mathbf{U}(s) = \mathbf{U}(\mathbf{X}(s))$. Now the explicit expression for $\mathbf{N}$ is (Ribe 2001)

$$\mathbf{N} = 4\eta_2 h\Delta\mathbf{s} + \frac{\eta_2}{3}(h^3\omega')'\mathbf{z}, \tag{14}$$

where $\Delta = \mathbf{U}' \cdot \mathbf{s}$ is the stretching rate of the mid-surface, $\omega = \mathbf{U}' \cdot \mathbf{z}$ is the rotation rate of the mid-surface, and $\mathbf{s}$ and $\mathbf{z}$ are unit vectors parallel to and perpendicular to the mid-surface, respectively. Because $\mathbf{U}$ appears both inside and outside the integral in eq. (13), the latter is a Fredholm integral equation of the second kind for $\mathbf{U}(s)$. The singular Green's function $\mathbf{J}$ must satisfy the conditions of vanishing normal flow and shear traction on the surface of the half-space. The form that ensures this is

$$J_{ij}(\mathbf{y}-\mathbf{x}) = J^{\star}_{ij}(\mathbf{y}-\mathbf{x}) + (-1)^{j+1} J^{\star}_{ij}(\mathbf{y}-\mathbf{x}^{\mathrm{IM}}), \tag{15}$$

where $\mathbf{x}^{\mathrm{IM}} \equiv \mathbf{x} - 2x_2\mathbf{e}_2$ is the mirror image of the point $\mathbf{x}$ across the boundary $x_2 = 0$ and

$$J^{\star}_{ij}(\mathbf{r}) = \frac{1}{4\pi}\left(-\delta_{ij}\ln|\mathbf{r}| + \frac{r_i r_j}{|\mathbf{r}|^2}\right) \tag{16}$$

is the Green's function for an infinite space. Finally, the evolution of the sheet's geometry is described by the kinematic equations

$$\frac{\mathrm{D}\mathbf{X}}{\mathrm{D}t} = \mathbf{U}, \qquad \frac{\mathrm{D}h}{\mathrm{D}t} = -h\Delta. \tag{17}$$

3 COMPARISON WITH THE BOUNDARY-ELEMENT METHOD

To validate BITS, we now compare its predictions with simulations performed using the BEM. To solve the BITS integral eqs (13)–(16), we employed a discrete Lagrangian numerical method that has been used successfully for slender fluid threads (Audoly *et al.* 2013). The discrete formulation begins by representing the sheet as a set of vertices connected by edges (Fig. A1). Certain variables (e.g. the velocities) naturally reside on the vertices, and others (e.g. the stretching rate) on the edges. The Lagrangian approach treats the vertices as material points, the positions of which are followed through time. These two aspects of the numerical method are discussed more thoroughly in Appendices A and B.

We begin with a vertical sheet of length $20h$ whose uppermost extremity is a distance $10h$ below the upper surface $x_2 = 0$ of a fluid half-space. By symmetry, only the velocity component u_2 parallel to the sheet is non-zero. Fig. 2 shows $u_2(x_2)$ predicted by BITS (solid lines) and BEM (dashed lines), for three values of the viscosity ratio $\gamma = 1$, 10 and 10 000. The BITS predictions are within 5 per cent of those of BEM, except near the top end of the sheet for $\gamma = 10$ where the error is about 9 per cent.

Next we consider a horizontal sheet of length $20h$ at a depth $10h$ beneath the surface of the half-space. Fig. 3 shows the velocity distribution predicted by BITS for viscosity ratios $\gamma = 10$ and 10^5. As expected, the centre of the sheet with $\gamma = 10$ sinks faster than the extremities, due to the upward flow of the ambient fluid around them. For $\gamma = 10^5$, the sheet behaves nearly as a rigid body, with a variation in velocity of only 1 per cent between the centre and the extremities.

Fig. 4 compares the BITS and BEM predictions of the vertical velocity u_2 as a function of the horizontal coordinate x_1, for three viscosity ratios. In all cases, the two predictions agree to within a few per cent everywhere except near the ends, where BITS is in error by up to 15 per cent (for $\gamma = 10$). The error at the ends decreases monotonically with increasing γ.

It is also of interest to examine how the error of BITS scales with the thinness $h/L \equiv \epsilon \ll 1$ of the sheet. Fig. 5 shows the error of BITS relative to that of BEM for a horizontal sheet with $\gamma = 10^4$ and $d = L$ (depth equal to length). The errors are those of the vertical component of velocity at the ends of the sheet (Fig. 5a) and at its midpoint (Fig. 5b). The errors increase up to $\epsilon^{-1} = 30$, and decrease strongly thereafter as ϵ^{-n}, where the exponents $n = 3.7$ (part a) and 2.07 (part b) are calculated from the two rightmost points on the respective plots.

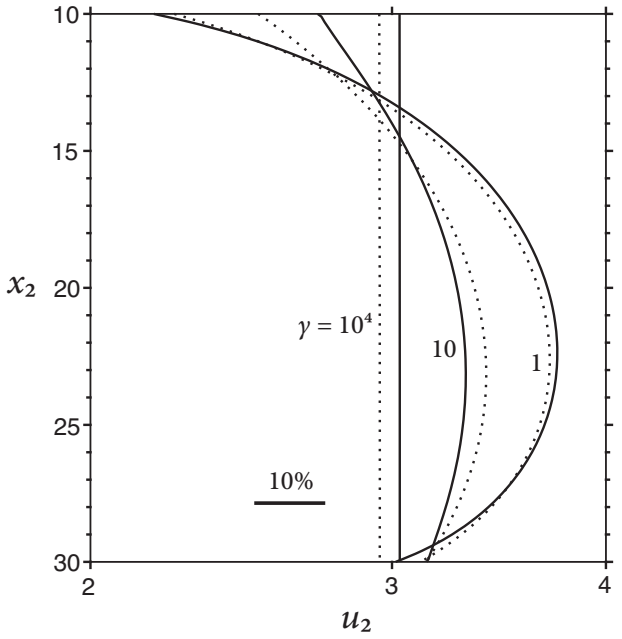

Figure 2. Vertical velocity of a vertical sheet $s \in [10h, 30h]$, for three different viscosity ratios $\gamma = 1$, 10 and 10^4. For each viscosity contrast, the BEM predictions are shown as dashed lines and the BITS predictions by solid lines. The horizontal bar indicates a difference of 10 per cent (note that the horizontal scale is logarithmic). The sheet is discretized with 201 points for the BITS solutions.

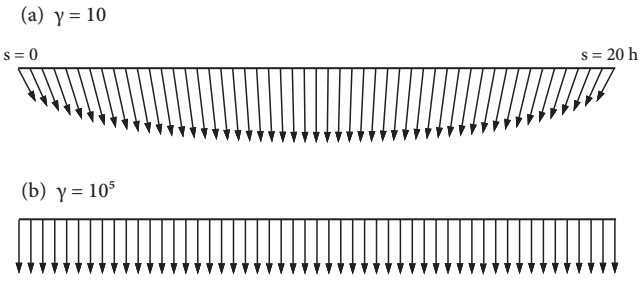

Figure 3. Velocity (arrows) as a function of position on the mid-surface of a horizontal sheet with $x_1 \in [0, 20h]$ and $x_2 = 10$, for two different viscosity ratios $\gamma = 10$ and 10^5. The maximum velocity in part (a) is $1.213h^2g\Delta\rho/\eta_1$.

Finally, we compare BITS to BEM for a case in which a sheet deforms for a finite time. Initially, a horizontal sheet of length $40h_0$ is located at a depth $d = 40h_0$ below the free surface, and then sinks for a time $t = 10\eta_1/h_0 g\delta\rho$. The notation h_0 here denotes the initial value of $h(s, t)$. Fig. 6 shows the shape (top) and thickness (bottom) of the sheet as predicted by BEM (left) and BITS (right). The calculated shapes are nearly identical, but BITS underpredicts the sinking distance by about 3 per cent (recalling that the starting depth is $40h_0$). BITS also underpredicts the sheet's stretching and shortening somewhat. At the midpoint $s = 0$, for example, the BITS prediction of the sheet's thickness is 4 per cent smaller than that of BEM.

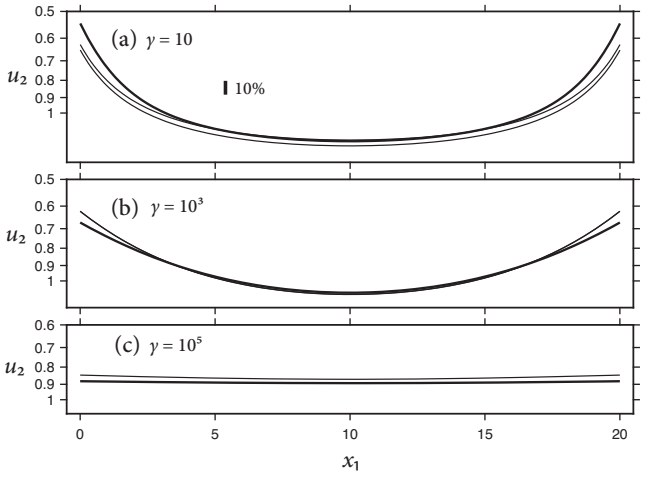

Figure 4. Vertical velocity u_2 as a function of position $x_1 \in [0, 20h]$ on a horizontal sheet at depth $10h$, for three different viscosity ratios $\gamma = 10$, 10^3 and 10^5. Thick lines: predictions of the BITS model. Thin lines: predictions of the BEM model. The two thin lines for $\gamma = 10$ indicate the slightly different velocities on the two surfaces of the sheet. The vertical bar in part (a) indicates a difference of 10 per cent (note that the vertical axis is logarithmic).

4 FREE SUBDUCTION: INSTANTANEOUS SOLUTIONS

Now that BITS has been found to be reasonably accurate, we use it to investigate the more subduction-like geometry shown in Fig. 1. BITS requires discretization of the sheet's mid-surface only, (dashed line in Fig. 1), whereas BEM would require discretization of both surfaces of the sheet as well as the rounded ends.

Ribe (2010) carried out a scaling analysis of the situation shown in Fig. 1, which predicts the following scaling law for the vertical sinking speed V of the slab's leading end:

$$\frac{V}{V_{\text{Stokes}}} = \text{fct(St)}, \qquad V_{\text{Stokes}} = \frac{h\ell g \Delta\rho}{\eta_1}, \qquad \text{St} = \frac{\eta_2}{\eta_1}\left(\frac{h}{\ell_b}\right)^3, \tag{18}$$

where ℓ_b is the 'bending length', St is the 'flexural stiffness' and V_{Stokes} is the characteristic sinking speed of a tabular object with characteristic thickness h and lateral dimension ℓ. The bending length is the length of the portion of the sheet where the bending moment is significant. In a geophysical context, it is the sum of the lengths of the slab and of the flexural bulge seaward of the trench.

Fig. 7 shows V/V_{Stokes} versus St for three values of the inclination θ_0 of the slab's leading end. The angle θ_0 is fixed for each diagram to ensure that the mid-surface be geometrically similar for all values of ℓ/h, which is a necessary condition for dynamical similarity. The points on each panel of Fig. 7 were obtained by solving the BITS equation for $\ell/h = 4$, 6 and 8, and the viscosity ratio $\gamma \in [30, 5 \times 10^5]$. In each panel the results collapse with minor error onto a universal master curve, indicating that the predicted form (18) is valid. Each master curve has two limits. For St ≤ 0.2, we have a 'Stokes' limit in which the slope of the curve is zero, indicating that the sinking speed is controlled entirely by the outer viscosity η_1. For St ≥ 10, we find a 'flexural' limit where the slope of the curve is -1, which implies that the sinking speed is controlled entirely by the viscosity η_2 of the sheet itself.

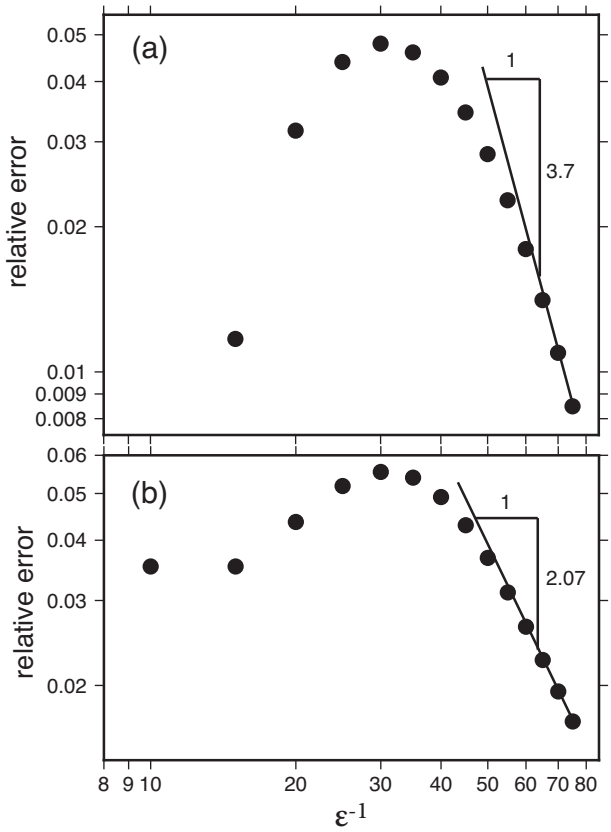

Figure 5. Error of the BITS algorithm relative to the predictions of the boundary-element method. The errors of the vertical velocity at the sheet's midpoint (a) and ends (b) are shown as functions of the thinness $h/L \equiv \epsilon$ for a horizontal sheet with $\gamma = 10^4$ whose length L is equal to its depth d. Different values of ϵ^{-1} are obtained by varying $L = d$.

5 FREE SUBDUCTION: TIME-DEPENDENT SOLUTIONS

Because inertia is negligible in the subduction process, time-dependence enters the problem only through the evolution equations (17) for the position of the mid-surface and the sheet's thickness. Fig. 8 shows the evolution of a sheet with $L = 40h$, $\ell = 6h$ and viscosity contrasts $\gamma = 100$ (left) and 1000 (right). For $\gamma = 100$, the inclination θ of the slab's leading edge is always less than 90° (Fig. 8a). This is because the 'mantle wind' around the slab edge easily bends the weak slab backwards, preventing it from reaching a vertical inclination. By contrast, a slab with $\gamma = 1000$ bends slightly beyond $\theta = 90°$, and then sinks quasi-vertically.

Fig. 8 also shows the thickness of the sheet as a function of time. For $\gamma = 100$, the maximum thinning of the slab is about 20 per cent (Fig. 8b). For $\gamma = 1000$, however, the maximum thinning is only a few per cent (Fig. 8d.)

6 CONCLUSIONS AND PERSPECTIVES

We have derived a new hybrid BITS equation that includes all the forces acting on a subducting sheet: gravity, viscous resistance to bending and stretching, and tractions applied by the ambient fluid. Comparison of the predictions of BITS with those obtained using the BEM shows that instantaneous solutions of BITS can be in error by up to 15 per cent near the ends of the sheet, where the small-slope approximation of BITS is not valid. However, the error near

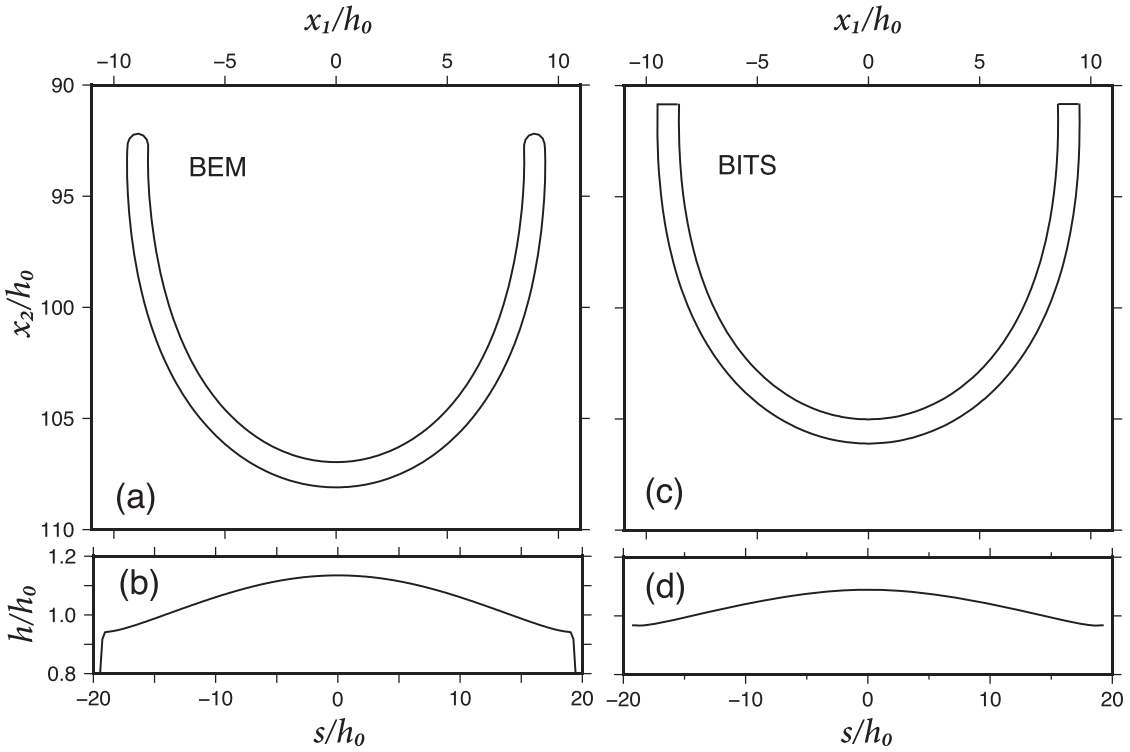

Figure 6. Comparison of solutions obtained by BEM (left) and BITS (right) for an initially horizontal sheet with viscosity ratio $\gamma = 100$ and length $40h_0$ located at a depth $40h_0$ below the free surface, and which sinks freely for a time $t = 10\eta_1/h_0 g\delta\rho$. The shape of the sheet is shown in parts (a) and (c), and its thickness as a function of arclength in parts (b) and (d).

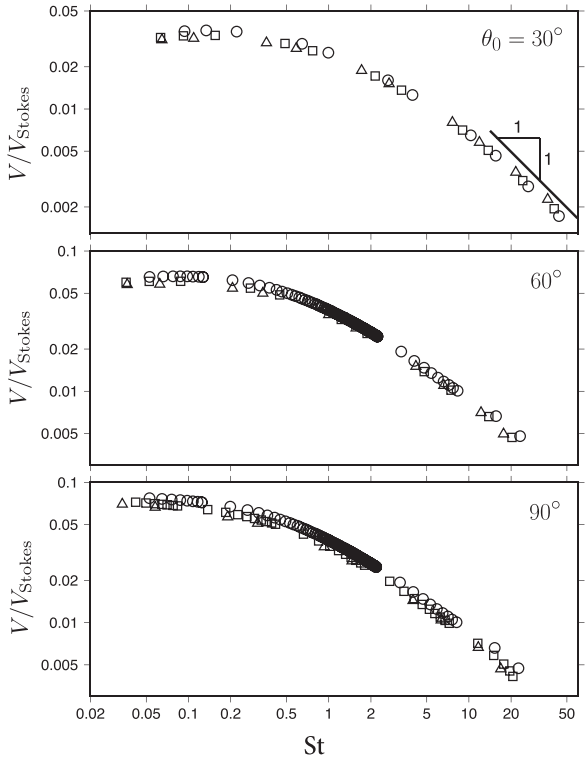

Figure 7. Normalized vertical sinking velocity of the slab's leading end as a function of the bending stiffness St, for three values of the inclination θ_0 of the leading end. Circles, squares and triangles are for $\ell/h = 4$, 6 and 8, respectively.

the ends is a decreasing function of the viscosity ratio γ, and is always <10 per cent for $\gamma \geq 100$. Away from the ends the errors are only a few per cent for moderate values of $L/h \equiv \epsilon^{-1} \in [10, 40]$. The error is maximum for $\epsilon^{-1} \approx 30$, and decreases rapidly for larger values of ϵ^{-1}.

We showed furthermore that BITS solutions for a subduction-like bent-sheet geometry (Fig. 1) obey the previously proposed (Ribe 2010) scaling law $V/V_{\text{Stokes}} = \text{fct(St)}$, where St is the sheet's flexural stiffness (Fig. 7). Finally, we showed that BITS can be used to predict the time evolution of an initially bent sheet for different viscosity ratios (Fig. 8). These results, together with the successful comparison of BITS with BEM, instill confidence that BITS captures the essential dynamics of subduction of a viscous sheet.

While we have only considered a single subducting sheet in this study, it is possible (but beyond our scope here) to extend BITS to two or more interacting sheets. In this context we take note of the study of Jagoutz *et al.* (2015), who use the semi-analytical formulation of Royden & Husson (2006) to develop a 'Fast Analytical Subduction Technique' (FAST) that can model the evolution of subduction systems comprising several interacting plates. However, the FAST approach does not use a boundary-integral representation of the Stokes equations.

At several points in this paper we have validated BITS by comparing its predictions to those of BEM. But does BITS have any advantages over BEM? The answer is a twofold yes. The first advantage is that only a single surface (the sheet's mid-surface) need be discretized, whereas BEM requires the discretization of the whole contour (= both surfaces plus the rounded ends of the sheet). The second and more important advantage is that BITS can be generalized to sheets with more realistic rheologies. For example, the rheology can be Newtonian but with a viscosity that varies along

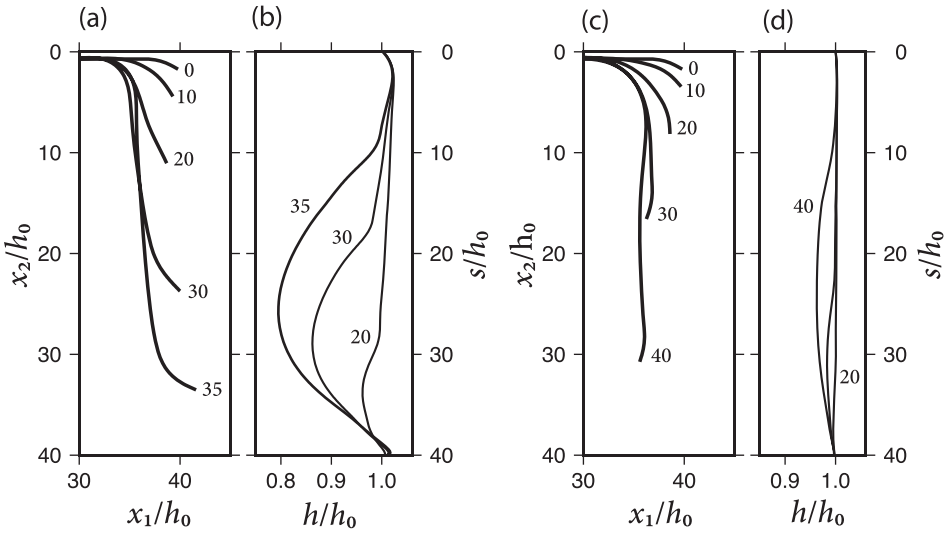

Figure 8. Evolution of slabs with viscosity ratio $\gamma = 100$ (left) and 1000 (right). Panels (a) and (c) show the shape of the slab at the dimensionless times $t\eta_1/h_0 g\delta\rho$ indicated, while panels (b) and (d) show the corresponding slab thickness as a function of arclength.

the sheet; or non-Newtonian with shear-thinning behaviour. This contrasts with the less flexible BEM approach, which requires each fluid domain to have a uniform Newtonian viscosity. We anticipate that generalized BITS models may prove fruitful for studying such phenomena as slab folding in the mantle transition zone and slab detachment. Work on these problems is underway and will be reported separately.

ACKNOWLEDGEMENTS

We thank B. Audoly for his aid with the discrete formulation of the BITS equation, and J. Chergui, D. Juric and B. Kaus for helpful discussions. We also thank two anonymous referees for careful and constructive reviews. Finally, B. Xu thanks the China Scholarship Council and the CNRS institute INSIS for financial support.

REFERENCES

Audoly, B., Clauvelin, N., Brun, P.-T., Bergou, M., Grinspun, E. & Wardetzky, M., 2013. A discrete geometric approach for simulating the dynamics of thin viscous threads, *J. Comput. Phys.,* **253,** 18–49.

Becker, T.W., Faccenna, C., O'Connell, R.J. & Giardini, D., 1999. The development of slabs in the upper mantle: insights from numerical and laboratory experiments, *J. geophys. Res.,* **104,** 15 207–15 226.

Bellahsen, N., Faccenna, C. & Funiciello, F., 2005. Dynamics of subduction and plate motion in laboratory experiments: insights into the plate tectonics behavior of the Earth, *J. geophys. Res.,* **110,** B01401, doi:10.1029/2004JB002999.

Faccenna, C., Heuret, A., Funiciello, F., Lallemand, S. & Becker, T.W., 2007. Predicting trench and plate motion from the dynamics of a strong slab, *Earth planet. Sci. Lett.,* **257,** 29–36.

Funiciello, F., Faccenna, C., Giardini, D. & Regenauer-Lieb, K., 2003. Dynamics of retreating slabs: 2. Insights from 3D laboratory experiments, *J. geophys. Res.,* **108,** B42207, doi:10.1029/2001JB000896.

Funiciello, F., Faccenna, C. & Giardini, D., 2004. Role of lateral mantle flow in the evolution of subduction systems: insights from 3-D laboratory experiments, *Geophys. J. Int.,* **157,** 1393–1406.

Funiciello, F., Faccenna, C., Heuret, A., Lallemand, S., Di Giuseppe, E. & Becker, T.W., 2008. Trench migration, net rotation and slab-mantle coupling, *Earth planet. Sci. Lett.,* **271,** 233–240.

Griffiths, R.W., Hackney, R.I. & van der Hilst, R.D., 1995. A laboratory investigation of effects of trench migration on the descent of subducted slabs, *Earth planet. Sci. Lett.,* **133,** 1–17.

Guillaume, B., Martinod, J. & Espurt, N., 2009. Variations of slab dip and overriding plate tectonics during subduction: insights from analogue modelling, *Tectonophysics,* **463,** 167–174.

Guillou-Frottier, L., Buttles, J. & Olson, P., 1995. Laboratory experiments on the structure of subducted lithosphere, *Earth planet. Sci. Lett.,* **133,** 19–34.

Jagoutz, O., Royden, L.H., Holt, A.F. & Becker, T.W., 2015. Anomalously fast convergence of India and Eurasia caused by double subduction, *Nat. Geosci.,* **8,** doi:10.1038/NGEO2418.

Kincaid, C. & Olson, P., 1987. An experimental study of subduction and slab migration, *J. geophys. Res.,* **92,** 13 832–13 840.

Ladyzhenskaya, O.A., 1969. *The Mathematical Theory of Viscous Incompressible Flow,* Gordon and Breach.

Li, Z. & Ribe, N.M., 2012. Dynamics of free subduction from 3-D boundary element modeling, *J. geophys. Res.,* **117,** B06408, doi:10.1029/2012JB009165.

Martinod, J., Funiciello, F., Faccenna, C., Labanieh, S. & Regard, V., 2005. Dynamical effects of subducting ridges: insights from 3-D laboratory models, *Geophys. J. Int.,* **163,** 1137–1150.

Morra, G., Regenauer-Lieb, K. & Giardini, D., 2006. Curvature of oceanic arcs, *Geology,* **34,** 877–880.

Morra, G., Chatelain, P., Tackley, P. & Koumoutsakos, P., 2007. Large scale three-dimensional boundary element simulation of subduction, *Int. Conf. Comp. Sci.,* Part III, LNCS 4489, 1122–1129.

Ribe, N.M., 2001. Bending and stretching of thin viscous sheets, *J. Fluid Mech.,* **433,** 135–160.

Ribe, N.M., 2010. Bending mechanics and mode selection in free subduction: a thin-sheet analysis, *Geophys. J. Int.,* **180,** 559–576.

Royden, L.H. & Husson, L., 2006. Trench motion, slab geometry and viscous stresses in subduction systems, *Geophys. J. Int.,* **167,** 881–905.

Schellart, W.P., 2004a. Kinematics of subduction and subduction-induced flow in the upper mantle, *J. geophys. Res.,* **109,** B07401, doi:10.1029/2004JB002970.

Schellart, W.P., 2004b. Quantifying the net slab pull force as a driving mechanism for plate tectonics, *Geophys. Res. Lett.,* **31,** L07611, doi:10.1029/2004GL019528.

Schellart, W.P., 2008. Kinematics and flow patterns in deep mantle and upper mantle subduction models: influence of the mantle depth and slab to mantle viscosity ratio, *Geochem. Geophys. Geosyst.,* **9,** Q03014, doi:10.1029/2007GC001656.

Torby, B.J., 1984. *Advanced Dynamics for Engineers,* Holt Rinehart & Winston.

APPENDIX A: LAGRANGIAN DESCRIPTION OF A THIN SHEET

It is convenient to express the variables of a thin sheet in a Lagrangian framework. Let t be the time, and S be the Lagrangian coordinate along the mid-surface at the initial time $t = 0$. For any variable $f(S, t)$, its time derivative is denoted by a dot,

$$\dot{f}(S,t) = \frac{\partial f(S,t)}{\partial t}. \tag{A1}$$

Let the mid-surface of the sheet be $\boldsymbol{X}(S, t)$. The material tangent $\boldsymbol{T}(S, t)$ is defined by

$$\boldsymbol{T}(S,t) = \frac{\partial \boldsymbol{X}(S,t)}{\partial S}. \tag{A2}$$

The norm of $\boldsymbol{T}(S, t)$ measures the amount of stretching of the centreline with respect to the reference configuration, and is used to define the unit tangent $\boldsymbol{t}$ of the centreline as

$$l(S,t) = |\boldsymbol{T}(S,t)|, \tag{A3}$$

$$\boldsymbol{t}(S,t) = \frac{\boldsymbol{T}(S,t)}{l(S,t)}. \tag{A4}$$

Then the Lagrangian axial stretching strain rate d is defined by

$$d(S,t) = \frac{\partial l(S,t)}{\partial t}. \tag{A5}$$

In the Lagrangian framework the velocity $\boldsymbol{U}$ is the time derivative of position:

$$\boldsymbol{U}(S,t) = \frac{\partial \boldsymbol{X}(S,t)}{\partial t}. \tag{A6}$$

A kinematic relation between the stretching strain rate $d(S, t)$ and the velocity $\boldsymbol{U}(S, t)$ is:

$$\begin{aligned} d(S,t) &= \frac{\partial l(S,t)}{\partial t} = \frac{1}{2l}\frac{\partial (l^2)}{\partial t} = \frac{1}{2l}\frac{\partial (\boldsymbol{T}^2)}{\partial t} \\ &= \frac{1}{l}\boldsymbol{T}\cdot\frac{\partial \boldsymbol{T}}{\partial t} = \boldsymbol{t}(S,t)\cdot\frac{\partial \boldsymbol{U}(S,t)}{\partial S}. \end{aligned} \tag{A7}$$

To describe the bending of the sheet, an orthonormal triad of vectors $\boldsymbol{d}_1(S, t)$, $\boldsymbol{d}_2(S, t)$, $\boldsymbol{d}_3(S, t)$ is introduced. The unit tangent vector $\boldsymbol{t}$ is identified with $\boldsymbol{d}_1(S, t)$, $\boldsymbol{d}_2(S, t)$ is the unit normal vector, and $\boldsymbol{d}_3(S, t)$ is a unit perpendicular vector out of the paper. The rates of change of the vectors $\boldsymbol{d}_i$ are

$$\frac{\partial \boldsymbol{d}_i(S,t)}{\partial t} = \boldsymbol{\omega}(S,t)\times\boldsymbol{d}_i(S,t) \tag{A8}$$

where $\boldsymbol{\omega}$ is the Darboux vector (angular velocity vector). Similarly, there is a second Darboux vector with respect to the space derivative:

$$\frac{\partial \boldsymbol{d}_i(S,t)}{\partial S} = \boldsymbol{\pi}(S,t)\times\boldsymbol{d}_i(S,t). \tag{A9}$$

The relation between $\boldsymbol{\omega}$ and $\boldsymbol{\pi}$ is known as the Maurer-Cartan identity:

$$\frac{\partial \boldsymbol{\omega}(S,t)}{\partial S} = \frac{\partial \boldsymbol{\pi}(S,t)}{\partial t} - \boldsymbol{\omega}(S,t)\times\boldsymbol{\pi}(S,t). \tag{A10}$$

The rotational strain rate can be written in terms of the first Darboux vector $\boldsymbol{\omega}$ as

$$\boldsymbol{e}(S,t) = \frac{\partial \boldsymbol{\omega}(S,t)}{\partial S}. \tag{A11}$$

The vector $\boldsymbol{e}$ describes the rates of rotational deformation by bending and twisting. For the 2-D sheet, there is no twisting but only bending around the vector $\boldsymbol{d}_3$, that is, the vector $\boldsymbol{d}_3$ is always same and keeps perpendicular to the paper:

$$\boldsymbol{\omega}(S,t) = \omega\boldsymbol{d}_3, \quad \boldsymbol{e}(S,t) = e\boldsymbol{d}_3, \tag{A12}$$

$$\boldsymbol{e}_b(S,t) = \boldsymbol{e}(S,t) = \frac{\partial \boldsymbol{\omega}(S,t)}{\partial S} \tag{A13}$$

where $\boldsymbol{e}_b$ is the bending strain rate.

Also, a simple explicit expression for the angular velocity for a 2-D sheet can be obtained:

$$\boldsymbol{\omega}(S,t) = \boldsymbol{t}(S,t)\times\dot{\boldsymbol{t}}(S,t). \tag{A14}$$

Eq. (A14) involves the time derivative of the unit tangent vector which can be derived from the permutation of derivatives with respect to t and S:

$$\dot{\boldsymbol{T}} = \frac{\partial}{\partial t}\left(\frac{\partial \boldsymbol{X}}{\partial S}\right) = \frac{\partial}{\partial S}\left(\frac{\partial \boldsymbol{X}}{\partial t}\right) = \frac{\partial \boldsymbol{U}}{\partial S}. \tag{A15}$$

At the same time, according to eq. (A4) we have $\dot{\boldsymbol{T}} = l\dot{\boldsymbol{t}} + \dot{l}\boldsymbol{t}$, whence the following relation is found:

$$l\dot{\boldsymbol{t}} + \dot{l}\boldsymbol{t} = \frac{\partial \boldsymbol{U}}{\partial S}. \tag{A16}$$

Expanding the cross product with $\boldsymbol{t}$, the angular velocity for a 2-D sheet becomes

$$\boldsymbol{\omega} = \boldsymbol{t}\times\dot{\boldsymbol{t}} = \frac{1}{l}\boldsymbol{t}\times(l\dot{\boldsymbol{t}}) = \frac{1}{l}\boldsymbol{t}\times(l\dot{\boldsymbol{t}} + \dot{l}\boldsymbol{t}) = \frac{1}{l}\boldsymbol{t}\times\frac{\partial \boldsymbol{U}}{\partial S}. \tag{A17}$$

In the Lagrangian framework, the internal viscous stress in the sheet can be described by a Rayleigh dissipation potential (Torby 1984). This potential has three contributions, corresponding to the stretching, bending and twisting modes of deformation. The utility of the Rayleigh potential $\mathcal{D}$ is that the net viscous force can be obtained by derivation with respect to the velocity. Thus, the resultant of the internal viscous stress on the mid-surface is

$$\boldsymbol{P}(S,t) = -\frac{\partial \mathcal{D}(S,t)}{\partial \boldsymbol{U}(S,t)}. \tag{A18}$$

Note that the quantity $\boldsymbol{P}$ is the net resultant per unit length dS in the Lagrangian configuration, and $\boldsymbol{P} = \partial \boldsymbol{N}/\partial S = l(\partial \boldsymbol{N}/\partial s)$. The expression of the dissipation potential in terms of the above kinematic variables will be derived in the following appendix for a Newtonian fluid.

So the BITS eq. (13) can be rewritten in the Lagrangian framework:

$$\begin{aligned} \boldsymbol{U}(S) = \frac{1}{\eta_2}\int_0^L &[\gamma \mathbf{g} l(R)h(R)\delta\rho + (\gamma-1)\boldsymbol{P}(R)] \\ &\cdot \boldsymbol{J}(\boldsymbol{X}(R) - \boldsymbol{X}(S))\mathrm{d}R, \end{aligned} \tag{A19}$$

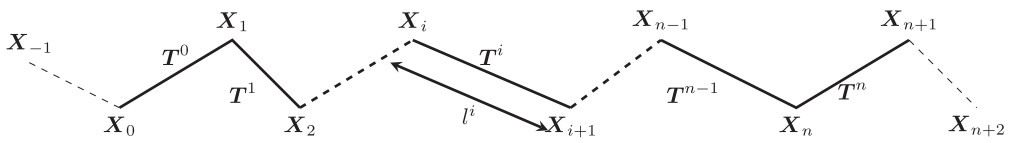

Figure A1. Discrete representation of a sheet as a set of vertices connected by edges.

where R is a dummy variable of integration representing arclength along the mid-surface.

Now eq. (A19) is non-dimensionalized using the initial plate thickness h_0 as the length scale, $h_0^2 g\delta\rho/\eta_1$ as the velocity scale and $\eta_1/h_0 g\delta\rho$ as the timescale. The dimensionless form of the integral eq. (A19) is

$$\boldsymbol{U}(S) = \frac{\gamma - 1}{\gamma}\int_0^{L/h_0} \boldsymbol{P}(R)\cdot\boldsymbol{J}(\boldsymbol{X}(R) - \boldsymbol{X}(S))\mathrm{d}R + \int_0^{L/h_0} l(R)h(R)\boldsymbol{e}_2\cdot\boldsymbol{J}(\boldsymbol{X}(R) - \boldsymbol{X}(S))\mathrm{d}R \tag{A20}$$

APPENDIX B: THE DISCRETE THIN VISCOUS-SHEET MODEL

In this section, discrete forms of the smooth equations discussed above are introduced, using concepts from discrete differential geometry developed by Audoly *et al.* (2013).

The first step is to represent the sheet's mid-surface by a collection of discrete vertices and connecting edges, as shown in Fig. A1. The positions of the $(n + 2)$ vertices are $\boldsymbol{X}_0(t), \boldsymbol{X}_1(t), \ldots, \boldsymbol{X}_{n+1}(t)$. The material tangent $\boldsymbol{T}$ becomes the segments between the vertices $\boldsymbol{T}^0(t), \boldsymbol{T}^1(t), \ldots, \boldsymbol{T}^n(t)$,

$$\boldsymbol{T}^i(t) = \boldsymbol{X}_{i+1}(t) - \boldsymbol{X}_i(t). \tag{B1}$$

Here and henceforth, subscripts and superscripts denote variables that are defined on vertices and edges, respectively.

The discrete segment length and unit tangent analogous to eqs (A3) and (A4) are

$$l^i(t) = |\boldsymbol{T}^i(t)|, \tag{B2}$$

$$\boldsymbol{t}^i(t) = \frac{\boldsymbol{T}^i(t)}{l^i(t)}. \tag{B3}$$

The velocities of the vertices are the time derivatives of the positions, or

$$\boldsymbol{U}_i(t) = \frac{\partial \boldsymbol{X}_i(t)}{\partial t}. \tag{B4}$$

In terms of the discrete variables, the discrete axial stretching strain rate for the segment $\boldsymbol{T}^i$ is

$$d^i(t) = \frac{\mathrm{d}l^i(t)}{\mathrm{d}t} = \boldsymbol{t}^i(t)\cdot\big(\boldsymbol{U}_{i+1}(t) - \boldsymbol{U}_i(t)\big). \tag{B5}$$

Comparing with eq. (A7) in the smooth case, we see that $d^i(t)$ is the integrated strain rate on the segment $\boldsymbol{T}^i$.

Similarly, the discrete analogue of eqs (A12) and (A17) is the following expression for the discrete bending strain rate on an interior vertex $\boldsymbol{X}_i$ $(1 \le i \le n)$:

$$\boldsymbol{e}_i^b(t) = \boldsymbol{\omega}^i(t) - \boldsymbol{\omega}^{i-1}(t), \tag{B6}$$

$$\boldsymbol{\omega}^i(t) = \boldsymbol{t}^i(t) \times \frac{\boldsymbol{U}_{i+1}(t) - \boldsymbol{U}_i(t)}{l^i(t)}. \tag{B7}$$

The discrete bending strain rate $\boldsymbol{e}_i^b$ is an integrated form of the smooth bending strain rate $\boldsymbol{e}^b(S, t)$. Note that the bending strain rate on vertex $\boldsymbol{X}_i$ involves the vertices $\boldsymbol{X}_{i-1}$, $\boldsymbol{X}_i$ and $\boldsymbol{X}_{i+1}$. So when the bending strain rates on the vertices $\boldsymbol{X}_0$ and $\boldsymbol{X}_{n+1}$ at the ends are calculated, extra vertices outsides the sheet are necessary. These extra vertices are called ghost vertices, and are shown in Fig. A1.

For the vertex $\boldsymbol{X}_0$ at the left end, we have:

$$\frac{\partial \boldsymbol{X}(S)}{\partial S} = \frac{-3\boldsymbol{X}_0 + 4\boldsymbol{X}_1 - \boldsymbol{X}_2}{2\Delta S} + O(\Delta S^2) = \frac{\boldsymbol{X}_1 - \boldsymbol{X}_{-1}}{2\Delta S} + O(\Delta S^2). \tag{B8}$$

In eq. (B8), the first form is a one-sided difference approximation and the second form is the usual second-order centred approximation involving the ghost vertex. Thus, from eq. (B8), the position of the ghost vertex at the left end is obtained as

$$\boldsymbol{X}_{-1} = 3\boldsymbol{X}_0 - 3\boldsymbol{X}_1 + \boldsymbol{X}_2. \tag{B9}$$

By the same method, the velocity on the left-end ghost vertex is

$$\boldsymbol{U}_{-1} = 3\boldsymbol{U}_0 - 3\boldsymbol{U}_1 + \boldsymbol{U}_2. \tag{B10}$$

Similar equations hold for the ghost vertex at the sheet's right end. With the ghost vertex $\boldsymbol{X}_{-1}$ and its velocity $\boldsymbol{U}_{-1}$, the quantities $\boldsymbol{t}^{-1}$, l^{-1}, $\boldsymbol{\omega}^{-1}$ on the ghost segment $\boldsymbol{T}^{-1}$ are given as for the interior segments and then we can get the bending strain rate $\boldsymbol{e}_0^b$ on vertex $\boldsymbol{X}_0$ by substituting $\boldsymbol{\omega}^{-1}$ into eq. (B6).

Now, other geometrical quantities and the modulus involved in the dissipation potential will be discretized. Each segment $\boldsymbol{T}^i$ carries an area A^i. This quantity is based on the initial segment length and thickness, and is conserved during a simulation in the Lagrangian framework. Thus, the thickness of each segment is

$$h^i(t) = \frac{A^i}{l^i(t)}. \tag{B11}$$

The length $\tilde{l}_i$ on a given interior vertex will be required later, and is defined as the average length of adjoining segments:

$$\tilde{l}_i(t) = \frac{l^{i-1}(t) + l^i(t)}{2} \quad (1 < i < n). \tag{B12}$$

The tilde symbol indicates a variable based on a vertex that is calculated from the average values on adjoining segments. Similarly, the area on a given vertex $\boldsymbol{X}_i$ can be obtained as

$$\tilde{A}_0 = \frac{A^0}{2}, \quad \tilde{A}_i = \frac{A^{i-1} + A^i}{2}, \quad \tilde{A}_{n+1} = \frac{A^n}{2}. \tag{B13}$$

By analogy with eq. (A18), the discrete net internal viscous resultant acting on the vertex $\boldsymbol{X}_i$ is given by

$$\boldsymbol{P}_i(t) = -\frac{\partial \mathcal{D}(t)}{\partial \boldsymbol{U}_i(t)}. \tag{B14}$$

Here, the net viscous resultant $\boldsymbol{P}_i$ is the integral of the quantity $\boldsymbol{P}$ in the smooth setting.

For convenience, all the positions and velocities on vertices are represented in the form of a matrix with the size $1 \times 3(n + 2)$:

$$\underline{X}(t) = \big(\boldsymbol{X}_0(t), \boldsymbol{X}_1(t), \ldots, \boldsymbol{X}_{n+1}(t)\big), \tag{B15}$$

$$\underline{U}(t) = \big(\boldsymbol{U}_0(t), \boldsymbol{U}_1(t), \ldots, \boldsymbol{U}_{n+1}(t)\big). \tag{B16}$$

So the expressions of the strain rates and the corresponding angular velocity vector can be rewritten with $\underline{X}$ and $\underline{U}$ in matrix form. Moreover, they are linear with respect to the velocity $\underline{U}$, whence

$$d^i(t) = \mathcal{L}_s^i(\underline{X}, \underline{U}) = \underline{U}\cdot\underline{\mathcal{L}}_s^i(\underline{X}), \tag{B17}$$

$$\boldsymbol{e}_i^b(t) = \underline{\mathcal{L}}_i^b(\underline{X}, \underline{U}) = \underline{U}\cdot\underline{\underline{\mathcal{L}}}_i^b(\underline{X}), \tag{B18}$$

$$\boldsymbol{\omega}^i(t) = \underline{\mathcal{W}}^i(\underline{X}, \underline{U}) = \underline{U} \cdot \underline{\underline{\mathcal{W}}}^i(\underline{X}). \tag{B19}$$

The size of the stretching strain rate matrix $\underline{\mathcal{L}}_s^i(\underline{X})$ is $3(n+2) \times 1$. The sizes of the bending strain rate matrix $\underline{\underline{\mathcal{L}}}_i^b(\underline{X})$ and the angular velocity matrix $\underline{\underline{\mathcal{W}}}^i(\underline{X})$ are both $3(n+2) \times 3$.

Since the stretching strain rate $d^i(t)$ only depends on the velocities $\boldsymbol{U}_i$ and $\boldsymbol{U}_{i+1}$ according to eq. (B5), the matrix $\underline{\mathcal{L}}_s^i(\underline{X})$ is sparse and has the following form:

$$\underline{\mathcal{L}}_s^i(\underline{X}) = \begin{pmatrix} \underline{0} \\ \hat{\underline{\mathcal{L}}}_s^i(\underline{X}) \\ \underline{0} \end{pmatrix}, \quad \hat{\underline{\mathcal{L}}}_s^i(\underline{X}) = (-\boldsymbol{t}^i, \boldsymbol{t}^i)^T. \tag{B20}$$

Here the matrix $\hat{\underline{\mathcal{L}}}_s^i(\underline{X})$, with the size 6×1, is the non-zero submatrix in the matrix $\underline{\mathcal{L}}_s^i(\underline{X})$ corresponding to the velocities $\boldsymbol{U}_i$ and $\boldsymbol{U}_{i+1}$.

Similarly, in view of eqs (B6) and (B7), the matrix $\underline{\underline{\mathcal{L}}}_i^b(\underline{X})$ and $\underline{\underline{\mathcal{W}}}^i(\underline{X})$ can be represented in the sparse matrix form

$$\underline{\underline{\mathcal{W}}}^i(\underline{X}) = \begin{pmatrix} \underline{\underline{0}} \\ \hat{\underline{\underline{\mathcal{W}}}}^i(\underline{X}) \\ \underline{\underline{0}} \end{pmatrix},$$

$$\hat{\underline{\underline{\mathcal{W}}}}^i(\underline{X}) = \frac{1}{l^i} \begin{pmatrix} 0 & -t^i[3] & t^i[2] \\ t^i[3] & 0 & -t^i[1] \\ -t^i[2] & t^i[1] & 0 \\ 0 & t^i[3] & -t^i[2] \\ -t^i[3] & 0 & t^i[1] \\ t^i[2] & -t^i[1] & 0 \end{pmatrix}, \tag{B21}$$

$$\underline{\underline{\mathcal{L}}}_i^b(\underline{X}) = \begin{pmatrix} \underline{\underline{0}} \\ \hat{\underline{\underline{\mathcal{L}}}}_i^b(\underline{X}) \\ \underline{\underline{0}} \end{pmatrix} = \underline{\underline{\mathcal{W}}}^i(\underline{X}) - \underline{\underline{\mathcal{W}}}^{i-1}(\underline{X}),$$

$$\hat{\underline{\underline{\mathcal{L}}}}_i^b(\underline{X}) = \hat{\underline{\underline{\mathcal{W}}}}^i(\underline{X}) - \hat{\underline{\underline{\mathcal{W}}}}^{i-1}(\underline{X}). \tag{B22}$$

The 6×3 non-zero submatrix $\hat{\underline{\underline{\mathcal{W}}}}^i(\underline{X})$ corresponds to the velocities $\boldsymbol{U}_i$ and $\boldsymbol{U}_{i+1}$. With the quantities on ghost vertices, the angular velocity matrix outside the sheet can be evaluated as

$$\hat{\underline{\underline{\mathcal{W}}}}^{-1} = \frac{1}{l^{-1}} \begin{pmatrix} 0 & -2t^{-1}[3] & 2t^{-1}[2] \\ 2t^{-1}[3] & 0 & -2t^{-1}[1] \\ -2t^{-1}[2] & 2t^{-1}[1] & 0 \\ 0 & 3t^{-1}[3] & -3t^{-1}[2] \\ -3t^{-1}[3] & 0 & 3t^{-1}[1] \\ 3t^{-1}[2] & -3t^{-1}[1] & 0 \\ 0 & -t^{-1}[3] & t^{-1}[2] \\ t^{-1}[3] & 0 & -t^{-1}[1] \\ -t^{-1}[2] & t^{-1}[1] & 0 \end{pmatrix},$$

$$\hat{\underline{\underline{\mathcal{W}}}}^{n+1} = \frac{1}{l^{n+1}} \begin{pmatrix} 0 & t^{n+1}[3] & -t^{n+1}[2] \\ -t^{n+1}[3] & 0 & t^{n+1}[1] \\ t^{n+1}[2] & -t^{n+1}[1] & 0 \\ 0 & -3t^{n+1}[3] & 3t^{n+1}[2] \\ 3t^{n+1}[3] & 0 & -3t^{n+1}[1] \\ -3t^{n+1}[2] & 3t^{n+1}[1] & 0 \\ 0 & 2t^{n+1}[3] & -2t^{n+1}[2] \\ -2t^{n+1}[3] & 0 & 2t^{n+1}[1] \\ 2t^{n+1}[2] & -2t^{n+1}[1] & 0 \end{pmatrix}. \tag{B23}$$

From the velocity on ghost vertices (B10), $\hat{\underline{\underline{\mathcal{W}}}}^{-1}$ and $\hat{\underline{\underline{\mathcal{W}}}}^{n+1}$ are seen to depend on $(\boldsymbol{U}_0, \boldsymbol{U}_1, \boldsymbol{U}_2)$ and $(\boldsymbol{U}_{n-1}, \boldsymbol{U}_n, \boldsymbol{U}_{n+1})$, respectively. Thus, the submatrix $\hat{\underline{\underline{\mathcal{L}}}}_i^b(\underline{X})$ involving three vertices $(i-1, i, i+1)$ has the size 9×3; the submatrices at the end vertices $\hat{\underline{\underline{\mathcal{L}}}}_0^b(\underline{X})$ and $\hat{\underline{\underline{\mathcal{L}}}}_{n+1}^b(\underline{X})$ with the same size 9×3 are one-side representations.

Now, the discrete internal viscous forces are arranged in matrix form $\underline{P}$ and then related to the dissipation and velocity matrices according to eq. (B14):

$$\underline{P} = \big(\boldsymbol{P}_0(t), \boldsymbol{P}_1(t), \ldots, \boldsymbol{P}_{n+1}(t)\big) = -\frac{\partial \mathcal{D}(t)}{\partial \underline{U}}. \tag{B24}$$

Thus, the non-dimensional discrete representation of the BITS eq. (A20) is

$$\begin{aligned} \boldsymbol{U}_i &= \frac{\gamma - 1}{\gamma} \sum_{j=0}^{n+1} (\boldsymbol{P}_j \cdot \boldsymbol{J}_{ij}) + \sum_{j=0}^{n+1} \big((\tilde{lh})_j \boldsymbol{e}_2 \cdot \boldsymbol{J}_{ij}\big) \\ &= \frac{\gamma - 1}{\gamma} \sum_{j=0}^{n+1} (\boldsymbol{P}_j \cdot \boldsymbol{J}_{ij}) + \sum_{j=0}^{n+1} (\tilde{A}_j \boldsymbol{e}_2 \cdot \boldsymbol{J}_{ij}), \end{aligned} \tag{B25}$$

where the Green's function $\boldsymbol{J}_{ij} = \boldsymbol{J}(\boldsymbol{X}_j - \boldsymbol{X}_i)$. Rewriting the discrete integral eq. (B25) in matrix form and substituting the net internal force (B24), we obtain

$$\underline{U} \cdot \underline{\underline{\delta}}_i - \frac{\gamma - 1}{\gamma} \underline{P} \cdot \underline{\underline{J}}_i = \underline{A} \cdot \underline{\underline{J}}_i, \tag{B26}$$

where, $\underline{\underline{\delta}}_i = (\underline{0}, \underline{0}, \ldots, \underline{I}, \ldots, \underline{0})^T$, $\underline{\underline{J}}_i = (\boldsymbol{J}_{i1}, \boldsymbol{J}_{i2}, \ldots, \boldsymbol{J}_{i(n+1)})^T$ and $\underline{A} = (\tilde{A}_1 \boldsymbol{e}_2, \tilde{A}_2 \boldsymbol{e}_2, \ldots, \tilde{A}_{n+1} \boldsymbol{e}_2)$.

Eq. (B26) is based on the vertex $\boldsymbol{X}_i$. Expanding it to all vertices yields the final matrix equation

$$\underline{U} - \frac{\gamma - 1}{\gamma} \underline{P} \cdot \underline{\underline{J}} = \underline{A} \cdot \underline{\underline{J}}, \tag{B27}$$

where $\underline{\underline{J}} = (\underline{\underline{J}}_1, \underline{\underline{J}}_2, \ldots, \underline{\underline{J}}_{n+1})$.

APPENDIX C: BENDING AND STRETCHING DISSIPATION POTENTIALS OF A NEWTONIAN SHEET

The general equations describing the low Reynolds number flow of a 2-D bent sheet are

$$\frac{\partial u}{\partial s} + \frac{\partial}{\partial z}(\kappa w) = 0, \tag{C1}$$

$$\frac{\partial \sigma_{ss}}{\partial s} + \frac{\partial}{\partial z}(\kappa \sigma_{zs}) + \sigma_{zs} \frac{\partial \kappa}{\partial z} = 0, \tag{C2}$$

$$\frac{\partial}{\partial z}(\kappa\sigma_{zz}) + \frac{\partial \sigma_{zs}}{\partial s} - \sigma_{ss}\frac{\partial \kappa}{\partial z} = 0, \tag{C3}$$

where σ_{ij} is the stress tensor and $\kappa = 1 - zK$. The components of the stress tensor are related to the velocity and pressure by

$$\sigma_{ss} = -p + \frac{2\eta_2}{\kappa}\Big(\frac{\partial u}{\partial s} - Kw\Big), \tag{C4}$$

$$\sigma_{zz} = -p + 2\eta_2\frac{\partial w}{\partial z}, \tag{C5}$$

$$\sigma_{zs} = \eta_2\Big[\frac{1}{\kappa}\frac{\partial w}{\partial s} + \kappa\frac{\partial}{\partial z}\Big(\frac{u}{\kappa}\Big)\Big]. \tag{C6}$$

The components σ_{sz}, σ_{zz} are small compared to the remaining components of the stress tensor, and can be set to zero:

$$\sigma_{sz} = \sigma_{zz} = 0. \tag{C7}$$

From eqs (C5)–(C7), we can obtain

$$\kappa\frac{\partial}{\partial z}\Big(\frac{u}{\kappa}\Big) = -\frac{1}{\kappa}\frac{\partial w}{\partial s}, \quad p = 2\eta_2\frac{\partial w}{\partial z}. \tag{C8}$$

According to the continuity equation,

$$\frac{\partial w}{\partial z} = -\frac{1}{\kappa}\Big(\frac{\partial u}{\partial s} - Kw\Big) \approx -\frac{1}{\kappa}\Big(\frac{\partial u}{\partial s} - KW\Big). \tag{C9}$$

Considering that the sheet is very thin, we assume that the velocity w varies little along the z-direction, that is, $\partial w/\partial s = \partial W/\partial s$. Thus, the first equation in eq. (C8) becomes

$$\kappa\frac{\partial}{\partial z}\Big(\frac{u}{\kappa}\Big) = -\frac{1}{\kappa}\frac{\partial W}{\partial s}. \tag{C10}$$

By integration of eq. (C10), the velocity u is found to be

$$u = -\frac{1}{K}\frac{\partial W}{\partial s} + C_2\kappa. \tag{C11}$$

When $z = 0$, eq. (C11) gives the velocity on the mid-surface $U(s) = -K^{-1}\partial W/\partial s + C_2$, so we can obtain $C_2 = -U(s) + K^{-1}\partial W/\partial s$. Thus, the velocity u is approximately

$$u = -z\frac{\partial W}{\partial x} + U\kappa. \tag{C12}$$

Substituting (C8), (C9) and (C12) into (C4), the remaining non-zero component of the stress tensor is

$$\begin{aligned}\sigma_{ss} &= \frac{4\eta_2}{\kappa}\left(\frac{\partial u}{\partial s} - KW\right) = \frac{4\eta_2}{\kappa}\Big(-z\frac{\partial W^2}{\partial^2 s} + \kappa\frac{\partial U}{\partial s} - KW\Big)\\ &= \frac{4\eta_2}{\kappa}(\Delta - z\omega'),\end{aligned} \tag{C13}$$

where $\Delta = U' - KW$ and $\omega = W' + KU$.

The rate of dissipation potential per unit length (into the page) of the sheet is

$$\phi(s) = \frac{1}{2}\int_{h/2}^{h/2} e_{ss}\sigma_{ss}\mathrm{d}z \approx \frac{1}{2}\Big[4\eta_2 h\Delta^2 + \frac{\eta_2 h^3}{3}(K\Delta - \omega')^2\Big]. \tag{C14}$$

The first term in eq. (C14) is the stretching dissipation potential and the second term is the bending dissipation potential:

$$\phi_s(s) = \frac{1}{2}\cdot 4\eta_2 h\Delta^2, \tag{C15}$$

$$\phi_b(s) = \frac{1}{2}\frac{\eta_2 h^3}{3}(K\Delta - \omega')^2 = \frac{1}{2}\frac{\eta_2 h^3}{3}\dot{K}^2, \tag{C16}$$

where $\dot{K} = \partial\omega/\partial s - K\Delta$ is the curling rate on the mid-surface, defined as the rate of change of the mid-surface curvature K. The bending dissipation potential (C16) suggests that the curling rate is a direct measure of the internal stresses that resist the bending of the sheet.

By analogy to the theory of elasticity, the stretching dissipation potential can be written in the form $\phi_s = D\Delta^2/2$, where the stretching modulus D is

$$D = 4\eta_2 h. \tag{C17}$$

Similarly, the bending dissipation potential can be defined as $\phi_b = B(\dot{K})^2/2$. Thus, the bending modulus B is

$$B = \frac{\eta_2 h^3}{3}. \tag{C18}$$

Now we can transform the dissipation potential expression into the Lagrangian description, whereupon the stretching rate Δ becomes $d(S, t)$ and the curling rate $\dot{K}$ becomes $e^b(S, t)$. The Rayleigh dissipation potential of the whole sheet is

$$\mathcal{D}(t) = \mathcal{D}_s(t) + \mathcal{D}_b(t), \tag{C19}$$

$$\mathcal{D}_s(t) = \int_0^L \frac{D(S,t)}{2l(S,t)}\big(d(S,t)\big)^2\mathrm{d}S, \tag{C20}$$

$$\mathcal{D}_b(t) = \int_0^L \frac{B(S,t)}{2l(S,t)}\big(\boldsymbol{e}^b(S,t)\big)^2\mathrm{d}S. \tag{C21}$$

Here, $D(S, t)$ and $B(S, t)$ are the Lagrangian stretching and bending moduli:

$$D(S,t) = 4\eta_2 h(S,t), \quad B(S,t) = 4\eta_2 I(S,t), \tag{C22}$$

where $I(S, t) = (h(S, t))^3/12$ is the moment of inertia about an axis in the mid-surface and in the $\boldsymbol{d}_3$ direction.

Based on the discrete geometrical quantities defined in Appendix B, the discrete stretching and bending moduli $D_i(t)$ and $B_i(t)$ are respectively

$$D^i(t) = 4\eta_2^i(t)h^i(t)/l^i, \tag{C23}$$

$$B_i(t) = 4\widetilde{\Big(\frac{\eta_2 I}{l}\Big)}_i(t). \tag{C24}$$

In (C24), $\widetilde{\big(\frac{\eta_2 I}{l}\big)}_i$ is defined on a vertex as the average of the values on adjoining segments:

$$\begin{aligned}&\widetilde{\Big(\frac{\eta_2 I}{l}\Big)}_0 = \frac{\eta_2^0 I^0}{l^0}, \quad \widetilde{\Big(\frac{\eta_2 I}{l}\Big)}_i = \frac{1}{2}\Big(\frac{\eta_2^{i-1} I^{i-1}}{l^{i-1}} + \frac{\eta_2^i I^i}{l^i}\Big),\\ &\widetilde{\Big(\frac{\eta_2 I}{l}\Big)}_{n+1} = \frac{\eta_2^n I^n}{l^n},\end{aligned} \tag{C25}$$

$$I^i = \frac{(h^i)^3}{12}, \tag{C26}$$

where I^i is the discrete moment of inertia. The dissipation potential can therefore be discretized as

$$\mathcal{D}_s(t) = \frac{1}{2}\sum_{0\le i\le n} D^i(t)\big(d^i(t)\big)^2 \tag{C27}$$

$$\mathcal{D}_b(t) = \frac{1}{2}\sum_{1\le i\le n} B_i(t)\big(\boldsymbol{e}_i^b(t)\big)^2. \tag{C28}$$

The dissipation potential is a quadratic function of the velocity $\underline{U}$. It can therefore be represented by a symmetric matrix

$$\mathcal{D}(t) = \frac{1}{2}\underline{U} \cdot \underline{\underline{\mathcal{D}}} \cdot \underline{U}, \tag{C29}$$

$$\underline{\underline{\mathcal{D}}} = \underline{\underline{\mathcal{D}}}_s + \underline{\underline{\mathcal{D}}}_b. \tag{C30}$$

Explicit expressions for these contributions can be found by substituting the matrix representations (B17)–(B22) into the expressions (C27) and (C28) of the discrete dissipation potential:

$$\begin{aligned} \underline{\underline{\mathcal{D}}}_s &= \sum_{0\le i\le n} \underline{\underline{\mathcal{D}}}^i_s = \sum_{0\le i\le n} D^i(t)\underline{\mathcal{L}}^i_s \otimes \underline{\mathcal{L}}^i_s, \\ \underline{\underline{\mathcal{D}}}^b &= \sum_{1\le i\le n} \underline{\underline{\mathcal{D}}}^b_i = \sum_{1\le i\le n} B_i(t)\underline{\underline{\mathcal{L}}}^b_i \cdot \left(\underline{\underline{\mathcal{L}}}^b_i\right)^T. \end{aligned} \tag{C31}$$

Thus, according to eqs (A18) and (C29), the matrix form of the net viscous resultant $\underline{P}$ can be simplified to

$$\underline{P} = -\frac{\partial \mathcal{D}(t)}{\partial \underline{U}} = -\underline{U} \cdot \underline{\underline{\mathcal{D}}} \tag{C32}$$

Substituting eq. (C32) into the discrete boundary-integral/thin-sheet eq. (B27), we obtain the matrix equation for a Newtonian sheet:

$$\underline{U} \cdot \left(\underline{\underline{I}} + \frac{\gamma - 1}{\gamma}\underline{\underline{\mathcal{D}}} \cdot \underline{\underline{J}}\right) = \underline{A} \cdot \underline{\underline{J}} \tag{C33}$$

By solving the matrix eq. (C33), the velocities on all vertices can be obtained.